Subwavelength and directional control of flexural waves in zone-folding induced topological plates

Rajesh Chaunsali, Chun-Wei Chen, and Jinkyu Yang*
Aeronautics and Astronautics, University of Washington, Seattle, Washington 98195-2400, USA

(Received 26 August 2017; published 13 February 2018)

Inspired by the quantum spin Hall effect shown by topological insulators, we propose a plate structure that can be used to demonstrate the pseudospin Hall effect for flexural waves. The system consists of a thin plate with periodically arranged resonators mounted on its top surface. We extend a technique based on the plane-wave expansion method to identify a double Dirac cone emerging due to the zone-folding in frequency band structures. This particular design allows us to move the double Dirac cone to a lower frequency than the resonating frequency of local resonators. We then manipulate the pattern of local resonators to open subwavelength Bragg band gaps that are topologically distinct. Building on this method, we verify numerically that a waveguide at an interface between two topologically distinct resonating plate structures can be used for guiding low-frequency, spin-dependent one-way flexural waves along a desired path with bends.

DOI: 10.1103/PhysRevB.97.054307

I. INTRODUCTION

A topological insulator has emerged as a new state of matter in condensed-matter physics. This is a special type of insulator that conducts electricity only on its boundary. Here topology is relevant because one can predict the boundary properties of these *finite* materials (i.e., finite-sized lattices) solely by knowing the bulk properties of *infinite* materials (i.e., infinitely large lattices). A topological framework provides an elegant way to categorize the bulk properties in terms of a topological invariant, and thus one expects a *topological protection* and a degree of *robustness* for the boundary properties [1,2].

Recently, this whole framework dealing with the flow of electrons has evolved further and influenced other areas, such as photonics [3] and acoustics [4–11]. It has also propelled a new design paradigm for artificial mechanical structures, so-called topological mechanical metamaterials, to achieve unconventional static (zero-frequency) [12–16] and dynamic (nonzero-frequency) [17–33] responses. In particular, tailoring nonzero-frequency responses, i.e., elastic waves in structures, on topological grounds shows tremendous potential to be used for energy harvesting, sensing, and impact mitigation purposes [34].

One of the most unique topological effects is the quantum spin Hall effect, the underlying phenomenon shown by topological insulators [35,36]. These systems are passive in the sense that they do not require any external field, but they still possess *directional* boundary states. This is due to the presence of Kramers partners, i.e., two opposite spins of an electron, which travel in the opposite directions on their boundaries, thereby keeping the time-reversal symmetry intact. Although mechanical counterparts, being bosonic systems, do not possess these intrinsic spins, one can carefully design the system to have two pseudospins by imposing certain symmetries in the lattice, and thus realize the pseudospin Hall effect [17,20,23,27,28].

While previous studies have successfully reported the feasibility of the pseudospin Hall effect in mechanical settings, in this study we focus on the feasibility of the same in less explored continuum structures such as plates. One of the approaches that has recently been applied in plate structures is a so-called zone-folding technique [37], in which one considers a larger unit cell rather than an irreducible one in a hexagonal lattice arrangement, so that the frequency band structure folds onto itself, creating a *double* Dirac cone at the Γ point. Based on the same, Brendel *et al.* [27] and Yu *et al.* [28] showed that purely geometric manipulation of holes can invoke topological effects in plates. However, these topological effects have been restricted to high-frequency wave modes. Therefore, in this research, we ask the following question: How can one invoke the pseudospin Hall effect at *low frequencies* for a given plate dimension? It is important because of several reasons: (i) the low-frequency plate modes, such as flexural modes, carry a large amount of energy, and manipulating them could lead to relevant engineering applications; and (ii) these lower modes generally require bigger lattice patterns of holes on conventional plates due to the Bragg condition, and thus an improved way of controlling the low-frequency wave modes can relax the current stringent size limitations. Therefore, it would be a significant advancement to the current research trend if one could demonstrate a low-frequency pseudospin Hall effect in a continuum mechanical structure such as plates, which are ubiquitous in many engineering disciplines.

To address the aforementioned challenges, we propose a topological plate system that consists of a thin plate with periodically arranged local resonators mounted on its top surface. This locally resonant (LR) plate is reminiscent of sonic crystals [38]. Pal *et al.* [24] proposed such a structure for realizing the elastic analog of the quantum valley Hall effect. Building on a similar methodology, in this research we employ a technique based on a combination of the classical plate theory and the plane-wave expansion (PWE) method

*jkyang@aa.washington.edu

 ©2018 American Physical Society

[39–41] that enables fast and efficient calculation of the wave dispersion relation. Furthermore, we integrate into this scheme the zone-folding technique to create a double Dirac cone for flexural wave modes. As a result, we report that the double Dirac cone can be formed in low-frequency regimes by tuning the resonating frequency of the resonators. In this way, we can demonstrate a subwavelength characteristic of the proposed plate system, i.e., the lattice size of the LR plate being smaller than the wavelengths in the bare plate at operating frequencies. We then show that a purely geometric manipulation of the local resonator pattern results in the opening of topologically trivial and nontrivial subwavelength Bragg band gaps around the double Dirac cone. Building on these findings, we verify numerically—by using the finite-element method (FEM)—that a waveguide created at the interface of topologically distinct LR plates can guide low-frequency flexural waves along a designed path. Moreover, it shows a unique spin-dependent one-way propagation characteristic. Unlike the traditional plate-based waveguides studied in the past [42–52], we show that this LR topological plate system has the potential to guide one-way flexural waves along a path with multiple bends—generally challenging in topologically trivial waveguides.

The structure of this paper is as follows: In Sec. II, we describe the design of the topological plate. In Sec. III, we present the PWE method to calculate the dispersion relation. In Sec. IV, we show the zone-folding of bands and create a double Dirac cone in a subwavelength regime. In Sec. V, we show the formation of a band gap around the double Dirac cone by perturbing the pattern of resonators on the LR plate. This facilitates the system to transition from a topologically trivial state to a nontrivial state. In Sec. VI, we employ the FEM to show the existence of two local modes, each designated by a pseudospin (clockwise or counterclockwise), at the interface of topologically trivial and nontrivial lattices. In Sec. VII, we demonstrate the feasibility of guiding low-frequency flexural wave modes along a path with bends and having a spin-dependent one-way propagation characteristic. In Sec. VIII, we conclude this paper.

II. DESCRIPTION OF THE LOCALLY RESONANT TOPOLOGICAL PLATE

Our system consists of a thin plate on which multiple local resonators are attached to form a lattice arrangement (Fig. 1). The rhombus-shaped unit cell is of length a and consists of six resonators in a hexagonal arrangement [Fig. 1(a)]. Each resonator is at a distance R and rotationally symmetric from the center of the unit cell, showing the C_6 symmetry. $\vec{a}_1$ and $\vec{a}_2$ are the lattice vectors. We model the resonators as cylindrical heads attached to the plate with a thin neck [Fig. 1(b)]. To invoke the topological effects in the system, we will only vary radius R, keeping the C_6 symmetry intact in this unit cell.

As a substrate material, we choose an aluminum plate ($E = 77.6$ GPa, $\rho = 2730$ kg/m^3, $\nu = 0.352$) of thickness $h = 1$ mm with the unit cell of size $a = 45$ mm. The resonator neck is made of acrylic plastic ($E_{\text{neck}} = 3.2$ GPa) with $h_{\text{neck}} = 5$ mm and $d_{\text{neck}} = 2$ mm, whereas the resonator head is made of tungsten ($\rho_{\text{head}} = 19\,260$ kg/m^3) with $h_{\text{head}} = 14$ mm and $d_{\text{head}} = 9$ mm. The aforementioned material properties are based on nominal values of standard materials.

III. CALCULATION OF THE UNIT-CELL DISPERSION

We first evaluate the dispersion characteristics of the unit-cell design with six resonators for variable R. For fast calculations, we rely on the PWE method. Toward that end, we simplify the resonator design with a lumped mass ($m = \pi\rho_{\text{head}}d_{\text{head}}^2h_{\text{head}}/4$) connected to the plate with a linear spring ($\beta = \pi E_{\text{neck}}d_{\text{neck}}^2/4h_{\text{neck}}$). In this process, we neglect the bending motion of the resonators and only consider their motion in the out-of-plane z direction. The bending (and other modes) of resonators, though taken into account in full-scale models in later sections, does not affect the topological phenomenon in our system as those frequencies can be separated from the Dirac point we will be investigating, and they have minimal coupling with out-of-plane wave modes (see Appendix A). We have $h \ll a$, therefore the plate can be assumed to be thin [40], and the transverse motion of the plate can be calculated as per the classical plate theory (i.e., Kirchhoff-Love theory) [53]. Following the approaches taken by Pal *et al.* [24], Xiao *et al.* [41], and Torrent *et al.* [48], the governing equations for the time-harmonic vibration of the unit cell with angular frequency ω can be written as

$$D\nabla^4 w(\mathbf{r}) - \omega^2\rho h w(\mathbf{r}) = -\beta\sum_{\alpha}[w(\mathbf{R}_\alpha) - \tilde{w}(\mathbf{R}_\alpha)] \times \delta(\mathbf{r} - \mathbf{R}_\alpha), \tag{1a}$$

$$-\omega^2 m\tilde{w}(\mathbf{R}_\alpha) = \beta[w(\mathbf{R}_\alpha) - \tilde{w}(\mathbf{R}_\alpha)], \tag{1b}$$

where $D = Eh^3/12(1-\nu^2)$ represents the flexural rigidity of the plate, $\mathbf{r} = (x, y)$ denotes the generalized coordinate of the plate, $w(\mathbf{r})$ represents the transverse displacement of the plate, and $\tilde{w}(\mathbf{R}_\alpha)$ represents the displacement of the resonating masses attached at points $\mathbf{R}_\alpha$. We have $\alpha = 1,2,\ldots,6$ for six different resonating masses per unit cell, and $\delta(\mathbf{r} - \mathbf{R}_\alpha)$ is a delta function in two dimensions.

We introduce the following nondimensional angular frequency:

$$\Omega = \omega a^2\sqrt{\frac{\rho h}{D}}.$$

Also, the mass of the resonator can be normalized as

$$\gamma = \frac{m}{\rho A_c h},$$

where $A_c = \sqrt{3}a^2/2$ is the area of a unit cell. We can write the normalized resonance frequency of a resonator as $\Omega_r = a^2\sqrt{(\beta/m)\rho h/D}$.

Employing the PWE method, we write the displacement of the plate for a Bloch wave vector $\mathbf{K}$ as a superposition of multiple plane waves such that

$$w(\mathbf{r}) = \sum_{\mathbf{G}} W(\mathbf{G})e^{-i(\mathbf{K}+\mathbf{G})\cdot\mathbf{r}}, \tag{2}$$

where $W(\mathbf{G})$ is a plane-wave coefficient and $\mathbf{G}$ denotes the reciprocal-lattice vector given by $\mathbf{G} = p\mathbf{b}_1 + q\mathbf{b}_2$, in which p and q are integers, and $\mathbf{b}_1$ and $\mathbf{b}_2$ are the basis vectors of the reciprocal lattice. We truncate the summation with respect to $\mathbf{G}$

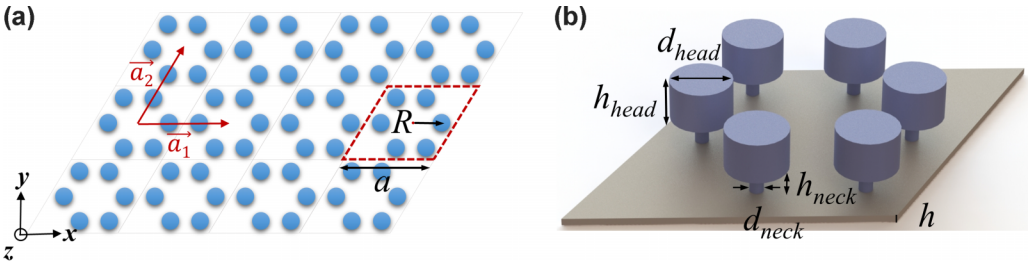

FIG. 1. (a) Lattice arrangement of the resonators with a rhombus-shaped unit cell in red. Dimensional parameters and lattice vectors are also shown. (b) A detailed view of the unit cell with six resonators mounted on top of a thin plate.

by choosing both p and q as $-M,-(M-1),\ldots,0,\ldots,(M-1),M$. Therefore, the reciprocal space is an $N\times N$ finite grid with $N=2M+1$.

The displacement of the plate at the locations where the resonators are attached can be simply deduced from Eq. (2) as

$$w(\mathbf{R}_\alpha)=\sum_{\mathbf{G}} W(\mathbf{G})e^{-i(\mathbf{K}+\mathbf{G})\cdot\mathbf{R}_\alpha}. \tag{3}$$

Substituting Eqs. (2) and (3) into Eq. (1a),

$$\begin{aligned} &D\sum_{\mathbf{G}'}|\mathbf{K}+\mathbf{G}'|^4W(\mathbf{G}')e^{-i(\mathbf{K}+\mathbf{G}')\cdot\mathbf{r}}-\omega^2\rho h\\ &\quad\times\sum_{\mathbf{G}'}W(\mathbf{G}')e^{-i(\mathbf{K}+\mathbf{G}')\cdot\mathbf{r}}\\ &=\beta\sum_{\alpha}\left[\tilde{w}(\mathbf{R}_\alpha)-\sum_{\mathbf{G}'}W(\mathbf{G}')e^{-i(\mathbf{K}+\mathbf{G}')\cdot\mathbf{R}_\alpha}\right]\delta(\mathbf{r}-\mathbf{R}_\alpha). \end{aligned} \tag{4}$$

Multiplying both sides with $e^{i(\mathbf{K}+\mathbf{G})\cdot\mathbf{r}}$, we obtain

$$\begin{aligned} &\sum_{\mathbf{G}'}[D|\mathbf{K}+\mathbf{G}'|^4-\omega^2\rho h]W(\mathbf{G}')e^{-i(\mathbf{G}'-\mathbf{G})\cdot\mathbf{r}}\\ &\quad=\beta\sum_{\alpha}e^{i(\mathbf{K}+\mathbf{G})\cdot\mathbf{r}}\left[\tilde{w}(\mathbf{R}_\alpha)-\sum_{\mathbf{G}'}W(\mathbf{G}')e^{-i(\mathbf{K}+\mathbf{G}')\cdot\mathbf{R}_\alpha}\right]\\ &\qquad\times\delta(\mathbf{r}-\mathbf{R}_\alpha). \end{aligned} \tag{5}$$

Taking the area integral over the entire unit cell of area A_c leads to

$$\begin{aligned} &\sum_{\mathbf{G}'}[D|\mathbf{K}+\mathbf{G}'|^4-\omega^2\rho h]W(\mathbf{G}')\iint_{A_c}e^{-i(\mathbf{G}'-\mathbf{G})\cdot\mathbf{r}}dr^2\\ &\quad=\beta\sum_{\alpha}\left[\tilde{w}(\mathbf{R}_\alpha)-\sum_{\mathbf{G}'}W(\mathbf{G}')e^{-i(\mathbf{K}+\mathbf{G}')\cdot\mathbf{R}_\alpha}\right]\\ &\qquad\times\iint_{A_c}e^{i(\mathbf{K}+\mathbf{G})\cdot\mathbf{r}}\delta(\mathbf{r}-\mathbf{R}_\alpha)dr^2. \end{aligned} \tag{6}$$

We now use the following relations:

$$\iint_{A_c}e^{-i(\mathbf{G}'-\mathbf{G})\cdot\mathbf{r}}dr^2=\begin{cases}A_c & \text{if } \mathbf{G}=\mathbf{G}',\\ 0 & \text{otherwise,}\end{cases} \tag{7a}$$

$$\iint_{A_c}f(\mathbf{r})\delta(\mathbf{r}-\mathbf{R}_\alpha)dr^2=f(\mathbf{R}_\alpha) \tag{7b}$$

to obtain

$$\begin{aligned} &A_c[D|\mathbf{K}+\mathbf{G}|^4-\omega^2\rho h]W(\mathbf{G})\\ &\quad=\beta\sum_{\alpha}\left[\tilde{w}(\mathbf{R}_\alpha)-\sum_{\mathbf{G}'}W(\mathbf{G}')e^{-i(\mathbf{K}+\mathbf{G}')\cdot\mathbf{R}_\alpha}\right]e^{i(\mathbf{K}+\mathbf{G})\cdot\mathbf{R}_\alpha}. \end{aligned} \tag{8}$$

Using Bloch's theorem for the resonators, we write $\tilde{w}(\mathbf{R}_\alpha)=\tilde{w}(\mathbf{0}_\alpha)e^{-i\mathbf{K}\cdot\mathbf{R}_\alpha}$, where $\tilde{w}(\mathbf{0}_\alpha)$ represents the Bloch displacement of the resonator (indexed with α) at the reference unit cell. Thus, we deduce

$$\begin{aligned} &[a^4|\mathbf{K}+\mathbf{G}|^4-\Omega^2]W(\mathbf{G})\\ &\quad=\gamma\Omega_r^2\sum_{\alpha}e^{i\mathbf{G}\cdot\mathbf{R}_\alpha}\left[\tilde{w}(\mathbf{0}_\alpha)-\sum_{\mathbf{G}'}W(\mathbf{G}')e^{-i\mathbf{G}'\cdot\mathbf{R}_\alpha}\right]. \end{aligned} \tag{9}$$

Similarly, we simplify the second governing Eq. (1b) (for $\alpha=1,2,\ldots,6$) as

$$-\Omega^2\tilde{w}(\mathbf{0}_\alpha)=\Omega_r^2\left[\sum_{\mathbf{G}}W(\mathbf{G})e^{-i\mathbf{G}\cdot\mathbf{R}_\alpha}-\tilde{w}(\mathbf{0}_\alpha)\right]. \tag{10}$$

Given the $N\times N$ size of the reciprocal space, we arrange Eqs. (9) and (10) in the form of an eigenvalue problem to solve for Ω at a specific Bloch wave vector $\mathbf{K}$ and obtain the dispersion relation. Note that we multiply Eq. (10) with γ to make the matrices Hermitian. Therefore, we have

$$\begin{bmatrix}\mathbf{P_{11}} & \mathbf{P}_{12}\\ \mathbf{P}_{21} & \mathbf{P}_{22}\end{bmatrix}\begin{Bmatrix}W(\mathbf{G})\\ \tilde{w}(\mathbf{0}_\alpha)\end{Bmatrix}=\Omega^2\begin{bmatrix}\mathbf{Q_{11}} & \mathbf{Q}_{12}\\ \mathbf{Q}_{21} & \mathbf{Q}_{22}\end{bmatrix}\begin{Bmatrix}W(\mathbf{G})\\ \tilde{w}(\mathbf{0}_\alpha)\end{Bmatrix} \tag{11}$$

with

$$\begin{aligned} \mathbf{P}_{11}=a^4&\begin{bmatrix}|\mathbf{K}+\mathbf{G}_1|^4 & 0 & \cdots & 0\\ 0 & |\mathbf{K}+\mathbf{G}_2|^4 & \cdots & 0\\ \vdots & \vdots & \ddots & \vdots\\ 0 & \cdots & 0 & |\mathbf{K}+\mathbf{G}_{N^2}|^4\end{bmatrix}\\ &+\gamma\Omega_r^2\exp\left\{i\begin{bmatrix}\mathbf{G_1}\\ \mathbf{G}_2\\ \vdots\\ \mathbf{G}_{N^2}\end{bmatrix}[\mathbf{R_1} \quad \mathbf{R}_2 \quad \cdots \quad \mathbf{R}_6]\right\}\\ &\times\exp\left\{-i\begin{bmatrix}\mathbf{R_1}\\ \mathbf{R}_2\\ \vdots\\ \mathbf{R}_6\end{bmatrix}[\mathbf{G_1} \quad \mathbf{G}_2 \quad \cdots \quad \mathbf{G}_{N^2}]\right\}, \end{aligned}$$

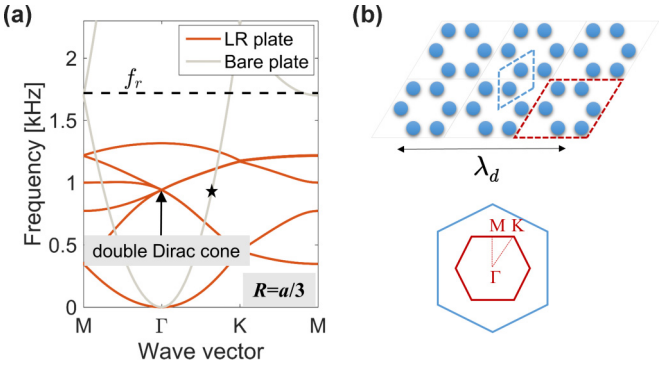

FIG. 2. (a) Dispersion plot for the LR plate with a hexagonal arrangement, i.e., $R = a/3$ (red curves). It shows a double Dirac cone, which is lower than the resonating frequency f_r of the local resonators. Dispersion of the bare plate with no local resonators is shown in light gray for comparison. (b) Two unit-cell representations to enable the zone-folding (i.e., mathematical folding) of bands and the corresponding Brillouin zones below. The smaller cell (enclosed by blue dashed lines) represents the typical, irreducible unit-cell configuration for the hexagonal arrangement, while in this study we consider the bigger unit cell (enclosed by red dashed lines) to create a double Dirac cone and for further topological manipulations. Their sizes are compared with the wavelength in the bare plate at the Dirac frequency (star mark), making it a subwavelength unit design.

$$\mathbf{P}_{12} = \mathbf{P}_{21}^{\dagger} = -\gamma\Omega_r^2 \exp\left\{ i \begin{bmatrix} \mathbf{G_1} \\ \mathbf{G}_2 \\ \vdots \\ \mathbf{G}_{N^2} \end{bmatrix} [\mathbf{R_1} \quad \mathbf{R}_2 \quad \cdots \quad \mathbf{R}_6] \right\},$$

$$\mathbf{P}_{22} = \gamma\Omega_r^2 \mathbf{I}_6,$$

$$\mathbf{Q}_{11} = \mathbf{I}_{N^2},\ \mathbf{Q}_{12} = \mathbf{Q}_{21}^{\dagger} = \mathbf{0}_{\{N^2,6\}},\ \mathbf{Q}_{22} = \gamma\mathbf{I}_6,$$

where exp, †, **I**, and **0** represent the exponential function, the conjugate transformation, the identity matrix, and the null matrix, respectively. We choose $N = 7$ for further calculations.

IV. BAND FOLDING AND SUBWAVELENGTH UNIT DESIGN

By using the aforementioned technique, we calculate the dispersion relation for the hexagonal arrangement of resonators, i.e., $R = a/3$ [see Fig. 1(a)], and we plot it in Fig. 2(a). Torrent *et al.* [48] showed the existence of a single Dirac cone in such a system. Building on this finding, in the current study we create a *double* Dirac cone (two Dirac cone dispersion curves superimposed) with the frequency $f_d = 0.94$ kHz at the Γ point. This is possible because we have chosen a bigger unit cell consisting of six resonators instead of two [compare the unit cells in Fig. 2(b) of different colors and corresponding Brillouin zones below]. This results in the dispersion curves folded onto a smaller Brillouin zone [37]. Note that the physics is the same in both representations and it is simply a *mathematical* zone-folding of bands. However, achieving a double Dirac cone—which is a key ingredient of the spin Hall systems—guides us to realize topological effects by manipulating the geometrical configuration of the larger unit cell (to be further discussed in Sec. V).

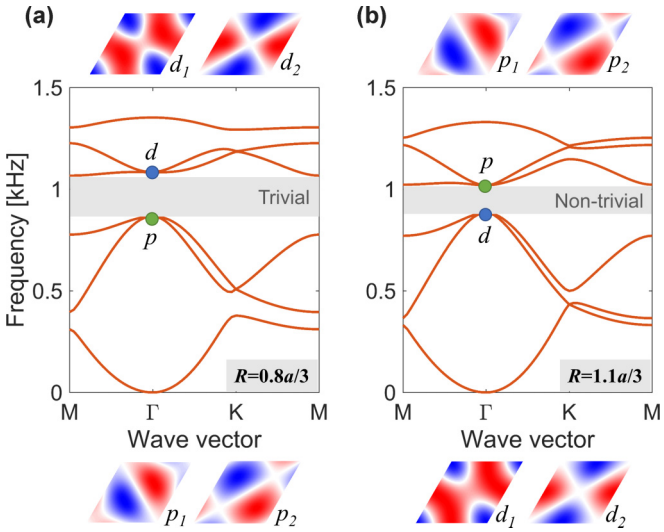

FIG. 3. Emergence of subwavelength Bragg band gaps and their inversion when the unit cell of the LR plate is perturbed around the $R = a/3$ configuration. (a) A case with $R < a/3$ leading to a topologically trivial band gap with p-type modes having lesser frequency than d-type modes. See the insets for the corresponding mode shapes, with the colors indicating the out-of-plane displacements of the plate. (b) A case with $R > a/3$ leading to a topologically nontrivial band gap with p- and d-type modes inverted.

In Fig. 2(a), we also mark the resonating frequency f_r of the local resonator. It equals $f_r = (1/2\pi)\sqrt{\beta/m} = 1.72$ kHz. It is important to realize that $f_d \leqslant f_r$, as was thoroughly investigated by Torrent *et al.* [48]. Therefore, the resonator design can be used as a tuning knob to push the Dirac frequency further down in the dispersion relation. In the same figure, we also plot the dispersion relation for a bare plate (i.e., the identical plate to the substrate described in Sec. II, but without local resonators attached). This is to compare the wavelength (λ_d) of the flexural wave in the bare plate if excited at the Dirac frequency. This is indicated by the star marker on the dispersion curve. For the chosen set of design parameters, λ_d is approximately 2.3 times longer than the length of the large unit cell (i.e., a), and 4 times longer than the size of the small, irreducible unit cell ($a/\sqrt{3}$). Figure 2(b) shows the relative sizes of the unit cells compared to this wavelength, indicating subwavelength units of the LR plate. Therefore, as the topological effects will be seen around the Dirac frequency, this opens up new pathways to controlling large-wavelength flexural waves by using a relatively small substrate. Again, by further reducing the resonant frequency, it is possible to shift the Dirac point to an even lower frequency regime, thereby making the plate design deep-subwavelength. However, practical challenges in designing such a system can limit the same, e.g., due to heavy resonating masses and soft neck structures.

V. BAND INVERSION AND TOPOLOGY

We now vary the radius R and see its effects on the wave dispersion in the system. For $R < a/3$, as shown in Fig. 3(a), there emerges a band gap near the Dirac frequency. We call it a subwavelength Bragg band gap because it lies in the

subwavelength regimes as discussed above but emerges due to the change in translational periodicity of the resonators. By keeping the C_6 symmetry intact, two modes on each side (the lower or higher side) of the gap are degenerate at the Γ point. Seen in the insets are the corresponding degenerate mode shapes of the plate at the Γ point, which are obtained by the PWE method described in Sec. III. Here, the lower-frequency modes are of p-type [p_1 and p_2 as shown in the bottom panel of Fig. 3(a)], and the higher-frequency modes are d-type [d_1 and d_2, upper panel in Fig. 3(a)] as per the analogy to electronic orbital shapes. For $R > a/3$, however, the band gap still exists, but its topological characteristic is different from the earlier case. As shown in Fig. 3(b), the degenerate modes are flipped, i.e., d-type modes are at the lower frequency compared to p-type modes. This *band inversion* as we vary R around $R = a/3$ indicates a typical topological transition in the system. Again, the validity of this result based on the lumped mass model is verified and discussed in Appendix A in comparison with the FEM (using COMSOL MULTIPHYSICS), which takes into account all geometrical features in the resonator design.

The presence of degenerate modes around the band gap has important implications in realizing the pseudospin Hall effect. One can take linear combinations of these modes and construct two alternate modes, i.e., pseudospin modes, without changing the physics of the system. Let $p_\pm = p_1 \pm ip_2$ and $d_\pm = d_1 \pm id_2$ represent such spin modes for these degenerate points. The sign in the middle determines if these are rotating clockwise or counterclockwise. We can interpret the dispersion near the Γ point in terms of the pair of spins by projecting the eigenstates onto the spin basis $\{p_\pm, d_\pm\}$. Therefore, the effective Hamiltonian of the system around the Γ point reduces to the one for the Cd/Te/HgTe/CdTe quantum well [36] and would resemble a mechanical pseudospin Hall system. One can show that the bands have a nonzero spin Chern number for the case with $R > a/3$, hence proving it to be topologically nontrivial [10,11,37].

VI. EMERGENCE OF THE TOPOLOGICAL INTERFACE STATE

Now that we verified the feasibility of the double Dirac cone formation and the band inversion in the unit-cell level, we move to the investigation of wave-guiding characteristics in multicell configurations. To account for more complicated geometry and boundary conditions in such a multicell setting, we resort to the FEM henceforth. According to the bulk-boundary correspondence of topology [1], we expect distinct behaviors on the boundaries of topologically trivial and nontrivial lattices. One way to observe it clearly is to have topologically distinct lattices placed adjacently and investigate their connecting interface for a nontrivial local response. Toward that end, we take a supercell, which consists of both topologically trivial ($R = 0.8a/3$) and nontrivial ($R = 1.1a/3$) lattices, 10 units of each placed as one strip [Fig. 4(a)]. The periodic boundary condition is introduced in the direction of another lattice vector (at 60° from the horizontal). In this way, such a system provides a quick way to calculate vibration responses at the interface and monitor their propagation along the periodic direction.

In Fig. 4(b), we plot the eigenfrequencies of the supercell as a function of wave number in the periodic direction. The

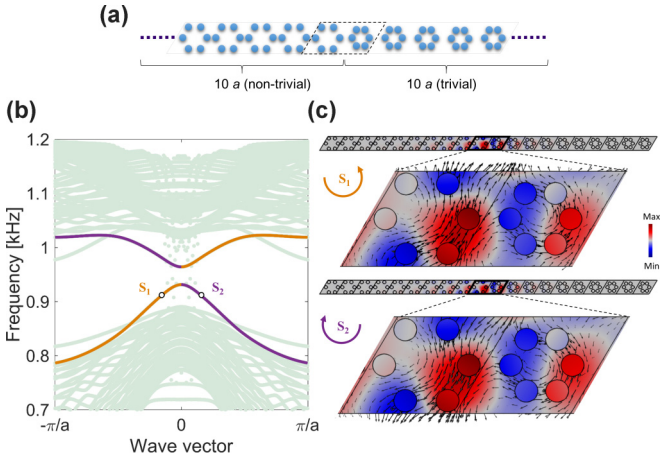

FIG. 4. (a) A supercell made by placing topologically distinct lattices adjacently. (b) Eigenfrequencies of the supercell as a function of the wave number in the periodic direction by analyzing a full-scale design with the FEM. We highlight clockwise (purple) and counterclockwise (yellow) pseudospin modes localized at the interface between the trivial and nontrivial lattices. In the background are the other modes, i.e., bulk modes, and local modes are at the extreme left and right end of the supercell. (c) Pseudospin mode shapes corresponding to the points S_1 and S_2 in (b). The color intensity represents the out-of-plane displacement, and the arrows indicate the time-averaged mechanical energy flux, thereby confirming their spin nature.

presence of two modes inside the band gap (shown in purple and yellow) is especially striking since those have the following nontrivial properties. First, they represent two types of pseudospin modes localized at the interface: one rotates clockwise while the other rotates counterclockwise. Second, both have opposite group velocities at a given frequency. Figure 4(c) shows the respective mode shapes corresponding to points S_1 and S_2 in Fig. 4(b), which are excited at 0.91 kHz. Opposite spins and group velocities of these modes can be verified by looking at the harmonic evolution of these modes (see Movie 1 in the Supplemental Material [54]). We also plot in-plane time-averaged mechanical energy flux ($I_j = -\sigma_{ij} v_j$, where σ_{ij} and v_j are the stress tensor and the velocity vector, respectively) over a harmonic cycle as black arrows. This further confirms the spin nature of these flexural modes in the LR plate.

There is a small frequency gap at the Γ point for these spin modes. The absence of topological interface modes indicates the absence of topological protection, which suggests these pseudospin modes are not topologically protected in the full frequency band gap. This is because, in our system, the protection is guaranteed by the C_6 symmetry, which we break by introducing a sharp interface between topologically trivial and nontrivial lattices, thereby resulting in an avoided crossing at the Γ point. Nevertheless, we will show in the next section that these modes can still be used to build robust and directional waveguides. The remedy to reduce the gap at the Γ point is to minimize the effect of the C_6 symmetry breaking at the interface. This can be done in several ways, including (i) by choosing the radii of trivial and nontrivial configurations as close as possible, and (ii) by constructing a *graded* interface between two topologically distinct lattices (see Appendix B).

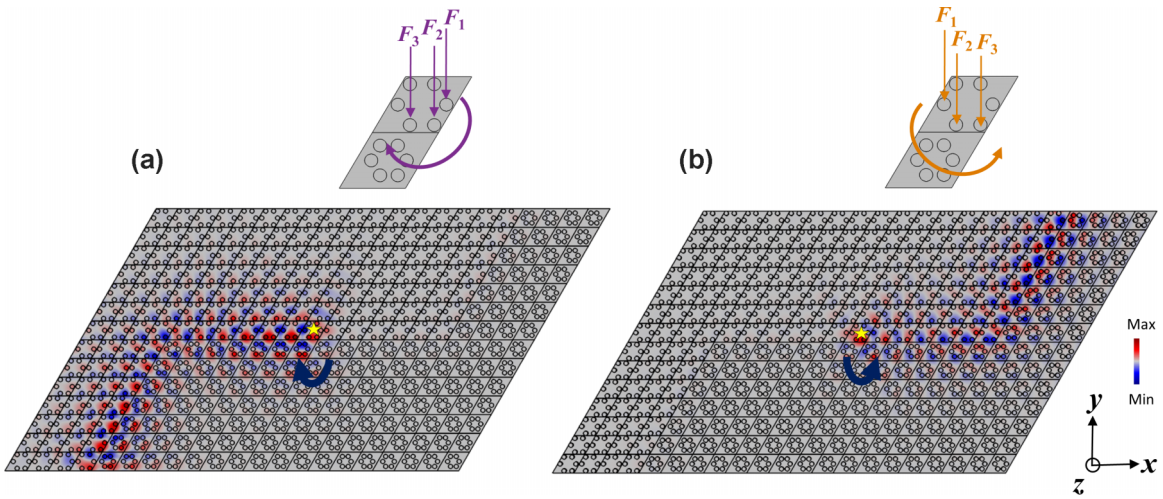

FIG. 5. Pseudospin dependent one-way propagation of a flexural wave. The star indicates the zone of excitation. Multipoint phased excitation in force is used for exciting (a) clockwise and (b) counterclockwise spin modes. The color intensity represents the out-of-plane displacement. No backscattering around the bends is observed.

This leads, therefore, to an enhanced degree of protection of the topological spin modes.

VII. DIRECTIONAL WAVEGUIDES

In the previous section, we showed that the mechanical spin Hall effect enables us to have two pseudospins at one frequency but in opposite directions. To demonstrate how this property can be used to build unconventional waveguides on plates, we combine topologically trivial and nontrivial LR plates to form a 2D structure. Figure 5 shows the waveguide (three linear segments with two bends) along the interface of two types of lattices. We give a forced excitation in the z direction at the center of the plate (indicated by the star symbol) in such a way that we selectively excite spin modes. This could be done, for example, by choosing multiple points in the vicinity but with a phase difference in their forcing. Insets show the three excitation points in a nontrivial unit cell (i.e., with $R = 1.1a/3$) where the spin is predominantly d-type. We extract the phase information from the spin modes in the supercell analysis done earlier for 0.91 kHz [see the resonators in red and blue, representing out-of-phase oscillations in Fig. 4(c)]. We apply this phased excitation as $F_1 = F\exp(i\omega t)$, $F_2 = F\exp(i\omega t + 2\pi/3)$, and $F_3 = F\exp(i\omega t + \pi)$. Note that the phase differences in the three excitation points are not equally spaced but show $\pi/3$ and $2\pi/3$ differences between the neighboring ones (i.e., $\pi/3$ between F_2 and F_3, and $2\pi/3$ between F_1 and F_2). This excitation tactic induces clockwise spin in Fig. 5(a) and counterclockwise spin in Fig. 5(b). We enforce low-reflecting boundary conditions on the plate and perform harmonic analysis using the FEM.

We confirm the unique features of this topological waveguide. The clockwise spin mode propagates to the left [Fig. 5(a)] and the counterclockwise spin propagates only to the right [Fig. 5(b)]. These spin waves propagate robustly along the waveguide interface in such a way that even though there are sharp bends, there is no backscattering and the spins remain intact (see Movie 2 in the Supplemental Material [54]). These simulation results imply that by using the pseudospin Hall effect induced in this LR plate structure, we can guide flexural waves in a selected path and direction without resorting to the breakage of time-reversal symmetry. That is, without using any active components, we can achieve directional control of low-frequency flexural waves simply by creating a topological boundary and exciting the host medium strategically via a phased excitation. It is important to note that the robustness of these spin waves shown along a waveguide with sharp bends does not imply that these are also robust against any other types of defects along the waveguide, as shown in acoustics recently [55]. Though our elastic LR plate structure demands a thorough stand-alone study on this subject in future, we have explored exemplary cases here in which certain defects along the waveguides can(not) backscatter these spin waves (Appendix C).

VIII. CONCLUSIONS

We have proposed a locally resonant plate structure to demonstrate the pseudospin Hall effect for directional control of flexural waves. We show that the resonator design can be simplified with a lumped mass model and solved by employing the plane-wave expansion method. This method enables us to efficiently investigate the key design parameters responsible for forming a double Dirac cone at a lower frequency than the resonating frequency of the local resonators. Keeping the C_6 symmetry intact, we perturb the unit cell and show an opening of subwavelength Bragg band gaps and the corresponding band-inversion process. This provides us with two topologically distinct lattice configurations. When these lattices are placed adjacently, we show the existence of two pseudospin modes traveling in the opposite directions along the interface. This unique feature is used to build topological waveguides with multiple bends and robustly guiding the spin-dependent flexural waves in a selected direction. The finding could be useful in designing compact and robust one-way channels for guiding low-frequency flexural waves in applications such as energy harvesting, sensing, and impact mitigation. Future studies include the optimization of the locally resonant plate

configurations by using the proposed numerical techniques, as well as the experimental verification of the waveguiding effects, which will be reported by the authors' future publications.

ACKNOWLEDGMENTS

We gratefully acknowledge fruitful discussions with Krishanu Roychowdhury (Cornell University), Rui Zhu (Beijing Institute of Technology), Raj Kumar Pal (Georgia Institute of Technology), Simon Yves (CNRS), Romain Fleury (EPFL), Cheng He (Nanjing University), Zhiwang Zhang (Nanjing University), and Panayotis Kevrekidis (University of Massachusetts, Amherst). We are grateful for the support from NSF (CAREER-1553202 and EFRI-1741685).

R.C. and C.-W.C. contributed equally to this work.

APPENDIX A: COMPARISON BETWEEN THE LUMPED MASS MODEL (PWE) AND THE FULL-SCALE MODEL (FEM)

We corroborate the results obtained earlier based on the lumped mass model now by using the FEM, in which we account for all geometrical features described in Fig. 1(b). As shown in Fig. 6, we clearly see excellent agreement between the PWE method (red curves) and the FEM (green circles). It should also be noted that the p- and d-type degenerate mode shapes obtained through the lumped mass model comply with those obtained by the full-scale model (compare the inset images between Figs. 3 and 6). In the dispersion relation obtained by the FEM, however, we observe that previously neglected shear-horizontal (SH_0) and shear (S_0) plate modes do appear for a thin plate. In our analysis, it is reasonable to ignore such modes and focus solely on antisymmetric (A_0) flexural modes for the transverse source excitation at low frequencies, as was already demonstrated by full-scale simulations in Secs. VI and VII. We also see nearly flat dispersion curves due to the other modes of local resonators, which were not accounted for in the lumped mass model. Nevertheless, these modes have minimal coupling with the out-of-plane vibration of the plate, and these are away from the double Dirac cone. Therefore, the band-inversion process is not affected by them and it is reasonable to neglect them in the PWE method.

APPENDIX B: GRADED INTERFACE BETWEEN TWO TOPOLOGICALLY DISTINCT LATTICES

Here we verify the scheme of reducing the gap observed at the Γ point in Fig. 4(b). The gap emerges due to the breakage of the C_6 symmetry at the interface. Therefore, we minimize the effect of symmetry breakage by modifying the interface. Figure 7(a) shows a supercell, in which a topologically nontrivial lattice ($R = 1.1a/3$) smoothly transitions to a topologically trivial lattice ($R = 0.8a/3$) via four lattices with a gradient in their radii, i.e., $R_1 = 1.05a/3$, $R_2 = 1.02a/3$, $R_3 = 0.95a/3$, and $R_4 = 0.9a/3$. The gap reduction is confirmed in Fig. 7(b). It is about three times smaller than the one observed in Fig. 4(b). The spin nature of these interface modes is also intact, as shown in Fig. 7(c).

APPENDIX C: THE PRESENCE OF DEFECTS ALONG THE WAVEGUIDE

We further examine the robustness of spin-dependent one-way flexural waves against certain defects present at the topological interface, as shown in Fig. 8. The first defect, i.e.,

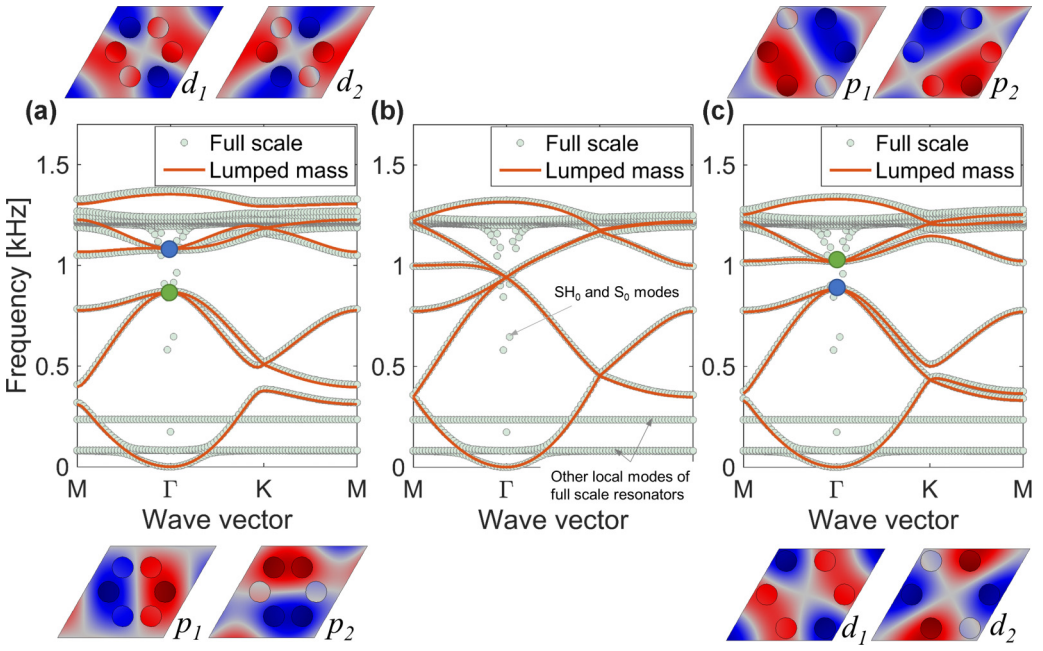

FIG. 6. Comparison of unit-cell dispersion curves obtained from the lumped mass model (solid curves) and the full-scale FEM (dotted curves) for the cases (a) $R = 0.8a/3$, (b) $R = a/3$, and (c) $R = 1.1a/3$. Excellent agreement is observed, and the band-inversion mechanism (insets with mode shapes obtained via the full-scale FEM) is confirmed for flexural modes (A_0). Additional modes emerging in the full-scale numerical simulation are SH_0 and S_0 guided plate modes, and other modes of local resonators.

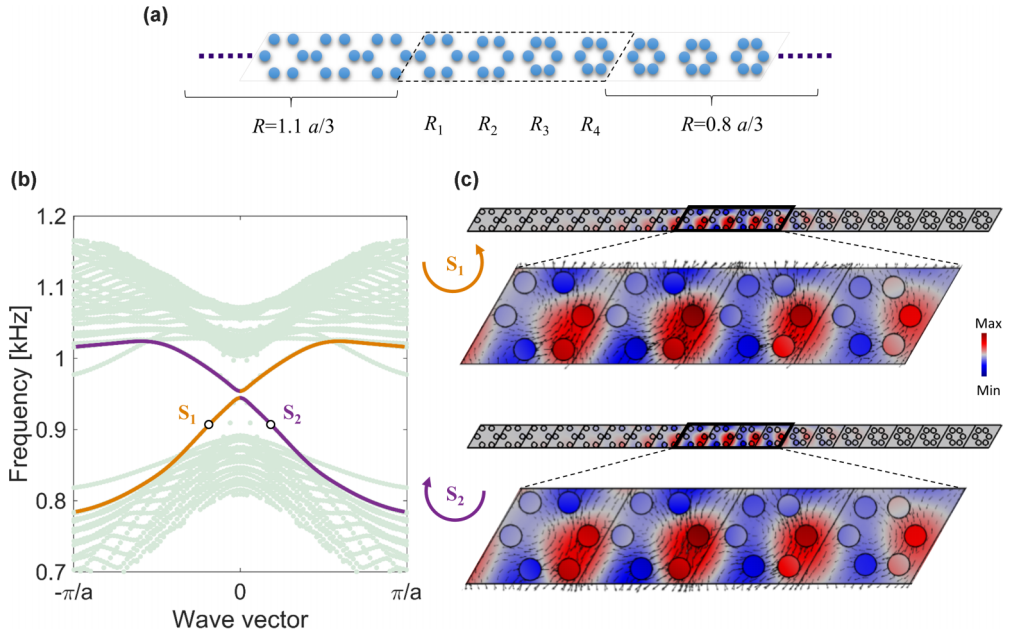

FIG. 7. The effect of a graded interface on the pseudospin modes at the interface. (a) A supercell with a smooth interface (radii $R_1 > R_2 > R_3 > R_4$) between topologically trivial and nontrivial lattices. (b) Eigenfrequencies of the modified supercell. The gap reduction at the Γ point can be observed, indicating a greater degree of topological protection. (c) Pseudospin modes corresponding to S_1 and S_2 points in the dispersion curve.

Defect 1, is introduced by removing four local resonators from one of the topologically trivial unit cells along the interface [see Fig. 8(a)]. We then excite a point on the leftmost end of the waveguide (shown by a star marker) with low-reflecting boundary conditions, and we perform harmonic analysis for the same frequency as that in Fig. 5. We observe that the presence of this defect does not have any noticeable effect in terms of scattering the spin mode. The mode continues to propagate from the left to the right with a counterclockwise spin [the same as in Fig. 5(b)] and maintains a similar modal amplitude before and after the defect location. Therefore, this defect would qualify as a non-spin-mixing defect [55].

We take another defect, i.e., Defect 2, in which we remove all six local resonators from the same unit cell [see Fig. 8(b)]. Thus this defect is "stronger" than Defect 1. Under the same excitation and boundary conditions as those in the previous

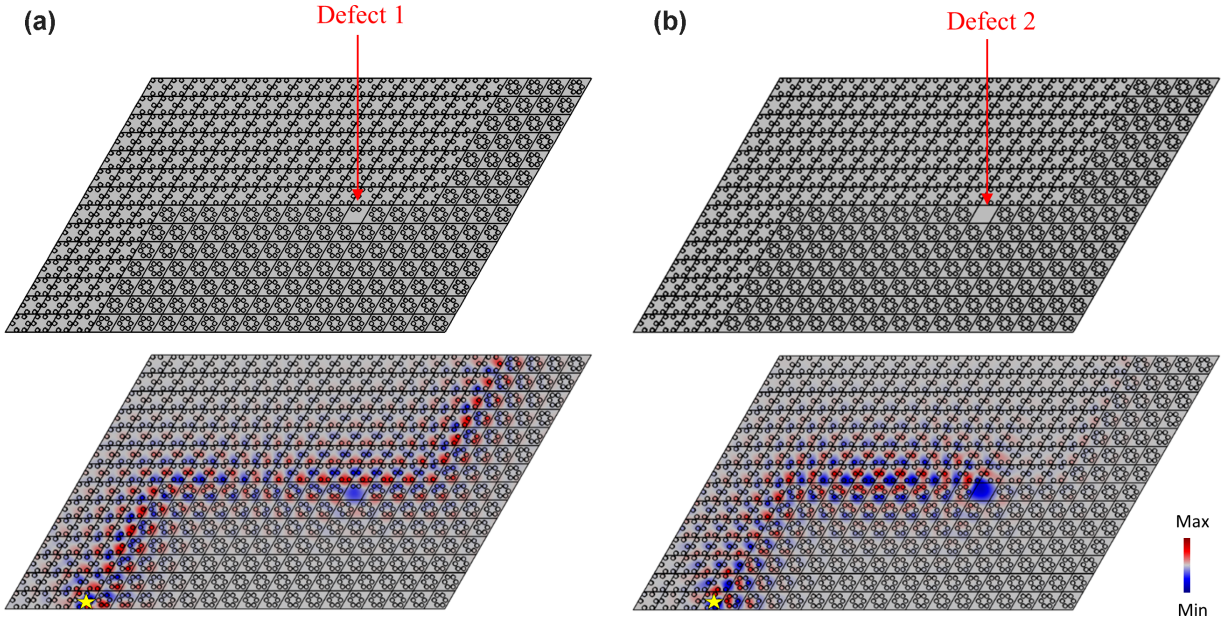

FIG. 8. The effect of defects on the spin-dependent one-way propagation of flexural waves. (a) Defect 1 is created by removing *four* resonators in one of the unit cells along the interface. The star indicates the point of excitation. No obvious backscattering is observed. (b) Defect 2 is created by removing *all six* resonators in the same unit cell. We observe backscattering of the spin mode from this defect.

case, we observe that this defect affects the spin mode more drastically. In Fig. 8(b), we see that the modal amplitude is almost negligible on the right side of the defect because of strong backscattering. The defect causes the spin modes to mix. Consequently, the rightward-propagating counterclockwise spin mode is converted to a leftward-propagating clockwise spin mode. Therefore, this represents a case of a spin-mixing defect [55].

[1] M. Z. Hasan and C. L. Kane, Rev. Mod. Phys. **82**, 3045 (2010).
[2] X. L. Qi and S. C. Zhang, Rev. Mod. Phys. **83**, 1057 (2011).
[3] L. Lu, J. D. Joannopoulos, and M. Soljačić, Nat. Photon. **8**, 821 (2014).
[4] M. Xiao, G. Ma, Z. Yang, P. Sheng, Z. Q. Zhang, and C. T. Chan, Nat. Phys. **11**, 240 (2015).
[5] Z. Yang, F. Gao, X. Shi, X. Lin, Z. Gao, Y. Chong, and B. Zhang, Phys. Rev. Lett. **114**, 114301 (2015).
[6] J. Lu, C. Qiu, M. Ke, and Z. Liu, Phys. Rev. Lett. **116**, 093901 (2016).
[7] C. He, X. Ni, H. Ge, X.-C. Sun, Y.-B. Chen, M.-H. Lu, X.-P. Liu, and Y.-F. Chen, Nat. Phys. **12**, 1124 (2016).
[8] J. Mei, Z. Chen, and Y. Wu, Sci. Rep. **6**, 32752 (2016).
[9] R. Fleury, A. B. Khanikaev, and A. Alù, Nat. Commun. **7**, 11744 (2016).
[10] Z. Zhang, Q. Wei, Y. Cheng, T. Zhang, D. Wu, and X. Liu, Phys. Rev. Lett. **118**, 084303 (2017).
[11] S. Yves, R. Fleury, F. Lemoult, M. Fink, and G. Lerosey, New J. Phys. **19**, 075003 (2017).
[12] C. L. Kane and T. C. Lubensky, Nat. Phys. **10**, 39 (2014).
[13] J. Paulose, B. G. Chen, and V. Vitelli, Nat. Phys. **11**, 153 (2015).
[14] D. Z. Rocklin, B. G.-G. Chen, M. Falk, V. Vitelli, and T. C. Lubensky, Phys. Rev. Lett. **116**, 135503 (2016).
[15] O. Stenull, C. L. Kane, and T. C. Lubensky, Phys. Rev. Lett. **117**, 068001 (2016).
[16] O. R. Bilal, R. Süsstrunk, C. Daraio, and S. D. Huber, Adv. Mater. **29**, 1700540 (2017).
[17] R. Süsstrunk and S. D. Huber, Science **349**, 47 (2015).
[18] L. M. Nash, D. Kleckner, A. Read, V. Vitelli, A. M. Turner, and W. T. M. Irvine, Proc. Natl. Acad. Sci. USA **112**, 14495 (2015).
[19] P. Wang, L. Lu, and K. Bertoldi, Phys. Rev. Lett. **115**, 104302 (2015).
[20] S. H. Mousavi, A. B. Khanikaev, and Z. Wang, Nat. Commun. **6**, 8682 (2015).
[21] T. Kariyado and Y. Hatsugai, Sci. Rep. **5**, 18107 (2015).
[22] Y.-T. Wang, P.-G. Luan, and S. Zhang, New J. Phys. **17**, 073031 (2015).
[23] R. K. Pal, M. Schaeffer, and M. Ruzzene, J. Appl. Phys. **119**, 084305 (2016).
[24] R. K. Pal and M. Ruzzene, New J. Phys. **19**, 025001 (2016).
[25] J. Vila, R. K. Pal, and M. Ruzzene, Phys. Rev. B **96**, 134307 (2017).
[26] C. Brendel, V. Peano, O. J. Painter, and F. Marquardt, Proc. Natl. Acad. Sci. USA **114**, E3390 (2017).
[27] C. Brendel, V. Peano, O. Painter, and F. Marquardt, Phys. Rev. B **97**, 020102(R) (2018).
[28] S.-Y. Yu, C. He, Z. Wang, F.-K. Liu, X.-C. Sun, Z. Li, M.-H. Lu, X.-P. Liu, and Y.-F. Chen, arXiv:1707.04901.
[29] G. Salerno, T. Ozawa, H. M. Price, and I. Carusotto, Phys. Rev. B **93**, 085105 (2016).
[30] C. L. Fefferman, J. P. Lee-Thorp, and M. I. Weinstein, Proc. Natl. Acad. Sci. USA **111**, 8759 (2014).
[31] R. Chaunsali, F. Li, and J. Yang, Sci. Rep. **6**, 30662 (2016).
[32] R. Chaunsali, E. Kim, A. Thakkar, P. G. Kevrekidis, and J. Yang, Phys. Rev. Lett. **119**, 024301 (2017).
[33] E. Prodan, K. Dobiszewski, A. Kanwal, J. Palmieri, and C. Prodan, Nat. Commun. **8**, 14587 (2017).
[34] S. D. Huber, Nat. Phys. **12**, 621 (2016).
[35] C. L. Kane and E. J. Mele, Phys. Rev. Lett. **95**, 226801 (2005).
[36] B. A. Bernevig, T. L. Hughes, and S.-C. Zhang, Science **314**, 1757 (2006).
[37] L.-H. Wu and X. Hu, Phys. Rev. Lett. **114**, 223901 (2015).
[38] Z. Liu, X. Zhang, Y. Mao, Y. Y. Zhu, Z. Yang, C. T. Chan, and P. Sheng, Science **289**, 1734 (2000).
[39] D.-L. Yu, G. Wang, Y.-Z. Liu, J. Wen, and J. Qiu, Chin. Phys. **15**, 0266 (2006).
[40] M. M. Sigalas and E. N. Economou, J. Appl. Phys. **75**, 2845 (1994).
[41] Y. Xiao, J. Wen, and X. Wen, J. Phys. D **45**, 195401 (2012).
[42] F. L. Hsiao, A. Khelif, H. Moubchir, A. Choujaa, C. C. Chen, and V. Laude, Phys. Rev. E **76**, 056601 (2007).
[43] Y. Pennec, B. Djafari-Rouhani, H. Larabi, J. O. Vasseur, and A. C. Hladky-Hennion, Phys. Rev. B **78**, 104105 (2008).
[44] Y. Pennec, B. D. Rouhani, H. Larabi, A. Akjouj, J. N. Gillet, J. O. Vasseur, and G. Thabet, Phys. Rev. B **80**, 144302 (2009).
[45] T. C. Wu, T. T. Wu, and J. C. Hsu, Phys. Rev. B **79**, 104306 (2009).
[46] M. Oudich, M. B. Assouar, and Z. Hou, Appl. Phys. Lett. **97**, 193503 (2010).
[47] F. Casadei, T. Delpero, A. Bergamini, P. Ermanni, and M. Ruzzene, J. Appl. Phys. **112**, 064902 (2012).
[48] D. Torrent, D. Mayou, and J. Sánchez-Dehesa, Phys. Rev. B **87**, 115143 (2013).
[49] X. P. Wang, P. Jiang, T. N. Chen, and J. Zhu, AIP Adv. **5**, 107141 (2015).
[50] P. Jiang, X. P. Wang, T. N. Chen, and J. Zhu, J. Appl. Phys. **117**, 154301 (2015).
[51] M. G. Baboly, A. Raza, J. Brady, C. M. Reinke, Z. C. Leseman, and I. El-Kady, Appl. Phys. Lett. **109**, 183504 (2016).
[52] Y. Chen, G. Hu, and G. Huang, J. Mech. Phys. Solids **105**, 179 (2017).
[53] F. Fahy and P. Gardonio, *Sound and Structural Vibration: Radiation, Transmission and Response*, 2nd ed. (Academic, Oxford, 2007).
[54] See Supplemental Material at http://link.aps.org/supplemental/10.1103/PhysRevB.97.054307 for movies depicting the harmonic evolution of topological interface modes for the supercell and full 2D plate analyses.
[55] Y. Deng, H. Ge, Y. Tian, M. Lu, and Y. Jing, Phys. Rev. B **96**, 184305 (2017).